International Journal of GEOMATE, July, 2024 Vol.27, Issue 119, pp.78-91
ISSN: 2186-2982 (P), 2186-2990 (O), Japan, DOI: https://doi.org/10.21660/2024.119.4395
Geotechnique, Construction Materials and Environment

CYCLIC LOADING TEST OF CLAMPED SPLIT POCKET MECHANISM AS A BEAM–COLUMN JOINT SYSTEM

Hamdi Yoga Pratama[1], *Angga Fajar Setiawan[1], Ashar Saputra[1], Iman Satyarno[1], and Whelly Trisya Putra[1]

[1]Department of Civil and Environmental Engineering, Universitas Gadjah Mada, Indonesia

*Corresponding Author, Received: 21 Jan. 2024, Revised: 23 April 2024, Accepted: 26 April 2024

ABSTRACT: This study evaluated the seismic performance of a clamped split pocket mechanism (CSPM) as a beam-column joint system for a prefabricated instant steel house. The CSPM utilizes a plug-and-play connection system with preloaded bolts, eliminating the need for on-site welding during assembly. Two full-scale CSPM specimens were examined for their stiffness, hysteretic behavior, skeleton curves, ductility, and failure modes using cyclic loading tests. The results indicated that the CSPM specimens exhibited a hysteretic response shape that appeared as a reverse S-shaped curve with pinching in the middle. Plastic deformation was formed through inelastic local buckling in the split pocket, which was crucial in absorbing seismic energy, effectively preventing brittle failure, and thereby reducing damage to the joint system. According to the criteria of AISC 341-16, the CSPM specimens were classified as partially restrained (PR) and ordinary moment frames (OMF) as their moment capacity did not surpass $0.8M_{max}$ at a rotation angle of 0.02 rad despite exhibiting adequate and stable lateral resistance in positive and negative loading directions up to 0.04 rad. This objective can be achieved with the condition that the beams and columns remain undamaged. Finally, the CSPM proved to be a reliable prefabricated beam-column joint system for a one-story instant steel house.

Keywords: Prefabricated Instant Steel House, Seismic Performance, Cyclic Loading, Bolts Preload, Post-Disaster Housing

1. INTRODUCTION

According to data from the National Disaster Management Agency (BNPB), earthquakes have inevitably occurred in regions classified as natural disasters in Indonesia for the past ten years. These include the Cianjur Earthquake (magnitude 5.6) in November 2022, which caused damage to 56,311 houses; the Palu Earthquake (magnitude 7.4) in September 2018, which damaged 68,451 houses; and the Lombok Earthquake (magnitude 7.0) in August 2018, which damaged 32,129 houses. Most of the damaged houses were attributed to poor construction, such as using brittle materials, inadequate reinforcement, and improper structural element configuration [1, 2]. After the earthquake, numerous houses became uninhabitable, thereby threatening the safety of inhabitants. This made the availability of decent housing with sufficient seismic resistance a major challenge during post-disaster reconstruction.

Prefabricated steel houses offer a viable solution to this problem, combining the speed of construction with the necessary seismic resistance to ensure safe and adequate housing during post-disaster reconstruction [1]. The prefabrication process offers notable advantages over traditional construction techniques, such as cost and time savings, improved quality control, and decreased dependence on skilled labor [3–5]. The advantages can be accomplished if all the main prefabricated structural components can be easily assembled through a simple connection design with accessible components and off-site welding [6, 7]. Furthermore, studies have shown that the connection design plays a crucial role in the seismic performance of prefabricated steel structures [8–10]. Therefore, developing simple steel connections with off-site welding that exhibit robust seismic performance is crucial.

Numerous studies have been conducted to investigate prefabricated steel connections that could be welded off-site. Bazarchi et al. [3] proposed a new male-female type interlocking connection with a tie plate and off-site welding to reduce the required on-site effort. However, a large slip occurred in the male-female components due to the removal of the uplift-constraining element. Zhang et al. [11] identified construction and performance flaws in existing modular connections, such as poor connectivity between modules and overly complex connecting mechanisms, which failed to meet seismic requirements. To mitigate these issues, they proposed a seismic retrofit solution involving self-centering haunch braces that effectively controlled damage and reduced deterioration in global strength. Cabaleiro et al. [12] investigated the behavior of steel joints using girder clamps in reconfigurable building structures, considering the amount of preload applied to the bolts. Their findings indicated that increasing the preload of bolts can considerably reduce joint deformation. Luo et al. [13] suggested a beam-to-column connection for steel-framed building modules using rectangular hollow sections and square hollow sections. Their study found that welded connections have high rotational stiffness and moment capacities

but exhibited brittle failure, whereas adding an end-plate stiffener improved stiffness, strength, and ductility. Chen et al. [14] introduced a novel connection design, incorporating a plug-in device and a long stay-bolt system at the ends of the beams with diagonal stiffeners. The experimental findings indicated that adding stiffeners effectively enhanced the load-bearing capacity, whereas the plug-in device facilitated easy assembly and eliminated on-site welding.

The easily assembled prefabricated steel structure can be improved on-site by employing the male and female connection method, incorporating hollow section elements. Fajar et al. [1] proposed a more straightforward clamped pocket mechanics using a mechanism of the male and female components of a circular hollow section. The proposed clamped pocket mechanics could resist sufficient friction-tension load because the pocket component gripped the beam and column using a clamping method induced by the bolt preloads. Ma et al. [15] developed a novel modular connection that allows ceiling and floor beams to fit naturally, eliminating the gap that caused the asynchronous movement of the twin beams. Their studies revealed that gaps between components and welding quantity were significant factors in overall joint behavior. Nadeem et al. [16] addressed the necessary workspace between construction modules, introducing a self-locking joint for modular steel structures. Although this solution effectively handled the bending moment at the joint, it led to shear stress on the male components due to load bearing. Khan and Yan [17] developed a novel prefabricated bolted joint for hollow structural sections (HSS) that exhibited adequate ductility. Nevertheless, the HSS column faced bearing failure against the beam bolts due to bending under quasistatic loading.

This study proposes a new beam-column connection, called clamped split pocket mechanism (CSPM), to address the limitations of existing prefabricated steel connections for earthquake-resistant instant house structures. The CSPM utilizes a plug-and-play connection system in which the beam and column fit into pockets, thereby eliminating the need for on-site welding. Afterwards, the beam and column are restrained using a clamping mechanism induced by preloaded bolts. To facilitate easy assembly, the column's pocket was split, and additional space was provided in other pockets to facilitate easy insertion of beams. Two experimental full-scale cyclic loading tests were conducted to evaluate the seismic performance of CSPM, encompassing stiffness evaluation, hysteretic behavior, skeleton curves, ductility performance, and failure modes while considering the effects of bending axis and splitting.

2. RESEARCH SIGNIFICANCE

The discussion above shows that the focus of previous studies on prefabricated steel connections has been mainly on modular buildings with relatively complex connection designs. However, there is a lack of research on prefabricated steel connections designed for post-disaster reconstruction with sufficient seismic resistance to withstand earthquakes, which is crucial to accelerate the fulfillment of the massive housing needs during post-disaster reconstruction. Therefore, there is an urgent need to address the specific requirements of such structures.

3. STRUCTURE OF THE CONNECTION

The CSPM connection system was critical for assuring the excellent seismic performance of prefabricated instant steel house structures. As depicted in Fig. 1, it could be implemented in the structure of a prefabricated instant steel house. The primary components of CSPM consisted of a double-lipped channel column, double-lipped channel beam, pocket, split pocket, clamp, stiffener, and preloaded bolts, as shown in Fig. 2. The beam and column utilized a double-lipped channel section (DLCS) configuration consisting of two-lipped channel sections joined together using welding spots at specific intervals. The pocket was a modified square hollow section (MSHS) designed to maintain an optimal space between the pocket and the beam. In contrast, the split pocket had a square hollow section divided into two parts, with its flanges modified, creating a C-shape section (CSS). The clamps attached to the pocket component were made from an angle section with standard-sized bolt holes.

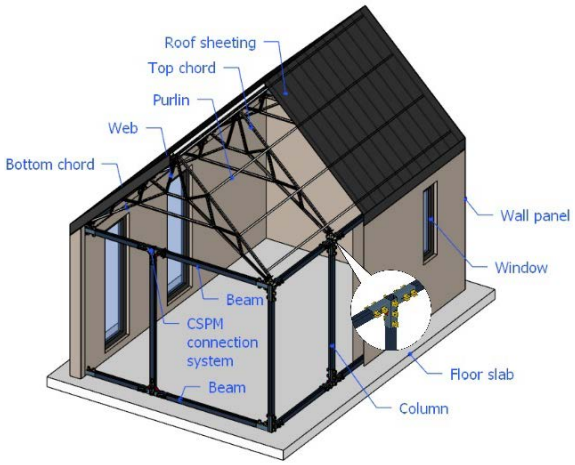

Fig. 1 Typical prefabricated instant steel house with the CSPM connection system

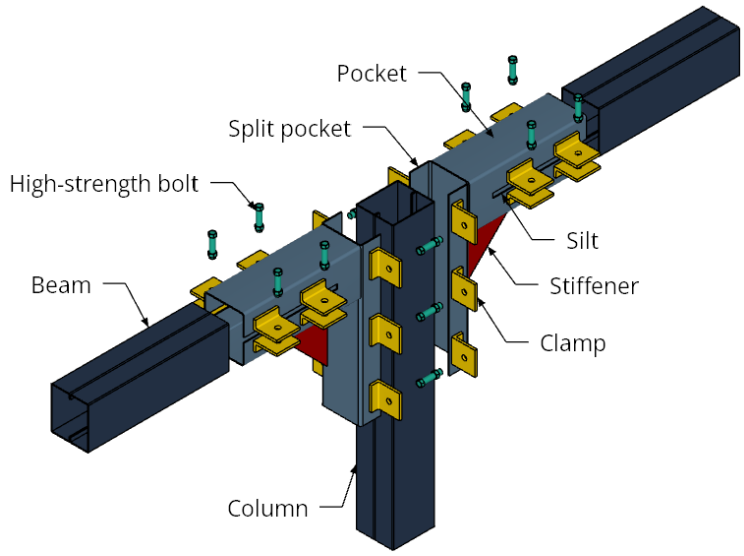

Fig. 2 The components of the CSPM connection system

The corner where the pocket and split pocket met was strengthened by a stiffener made from a steel plate. These components were prefabricated and welded together at the factory, and on-site assembly was possible using preloaded bolts.

4. EXPERIMENTAL DESIGN

4.1 Design of Specimens and Parameters

The seismic performance of CSPM was assessed using two test specimens. In one specimen, the DLCS was loaded along its strong axis, whereas in the other, it was loaded along its weak axis. Table 1 presents the detailed parameters for CSPM specimens. The sectional dimensions of CSS were 90 mm (depth, h_c) × 40 mm (flange width, b_c) × 1.65 mm (thickness, t_c) and 100 mm (depth, h_c) × 40 mm (flange width, b_c) × 1.65 mm (thickness, t_c) for the strong and weak axes, respectively. These dimensions were created differently, thereby allowing a split pocket to fit the column for each bending axis. Steel column and steel beam sections were DLCS with sectional dimensions of 95 mm (depth, h_d) × 80 mm (width, b_d) × 10 mm (lip length, l_d) × 1.9 mm (thickness, t_d). The pocket section was an MSHS with dimensions 100 mm (depth, h_m) × 90 mm (width, b_m) × 1.65 mm (thickness, t_m). A gap was present between the pocket and beam-column cross-section to facilitate assembly. To ensure that the pocket could still grip when subjected to a preload, a slit was provided on the pocket with a slit width greater than the gap width. This allowed the pocket to grip the beam and column securely. High-strength bolts with a diameter of 10 mm were used in all specimens. Except for the bolts, all components of the CSPM connection were coated with steel paint to ensure consistency. Furthermore, Fig. 3 provides the dimensions of other components associated with the CSPM connection, and Fig. 4 illustrates the specific dimensions of the CSPM specimens along the strong and weak axes.

4.2 Material Properties

The coupon specimens were extracted from two steel sections: MSHS and DLCS. These steel sections were made from hot-rolled mild steel, using the same batch of steel plates for their production. The dimensions of the coupon specimens followed the guidelines specified in JIS Z 2241 [18], which outlines the procedure for conducting tensile tests on metal. Each type of steel had two coupon specimens, resulting in four samples. The coupon tests were conducted, which yielded the stress-strain data. Fig. 8 depicts that the stiffness degradation of specimens CSPM-1 and CSPM-2 showed the same trend. The stiffness curve took on a curvilinear form, where the stiffness decreased linearly at the beginning, forming a curve at a certain rotation angle. Nonetheless, the stiffness between the positive and negative directions at the beginning of the linear phase had different values in both specimens. Specifically, the stiffness in the positive direction was lower than the negative direction at a rotation angle, presenting the average material property values obtained from the testing, including the yield strength (f_y) and the tensile strength (f_u).

4.3 Test Setup and Loading Protocol

All experiments were conducted by placing the test specimens in a horizontal position Fig. 5. depicts the loading configuration of the test setup. The testing apparatus consisted of the specimen, 250-kN horizontal actuator, load cell, linear variable differential transformer, pin supports, and concrete

Table 1. Parameters of the specimens

Specimen	Bending axis	Beam and column (mm)	Pocket		Split pocket		Stiffener (mm)	Bolt	
			Section (mm)	Length (mm)	Section (mm)	Length (mm)		Diameter (mm)	Preload (kN)
CSPM-1	Strong	DLCS 95 × 80 × 10 × 1.90	MSHS 100 × 90 × 1.65	250	CSS 90 × 40 × 1.65	335	100 × 100 × 2	10	5
CSPM-2	Weak	DLCS 95 × 80 × 10 × 1.90	MSHS 100 × 90 × 1.65	250	CSS 100 × 40 × 1.65	335	100 × 100 × 2	10	5

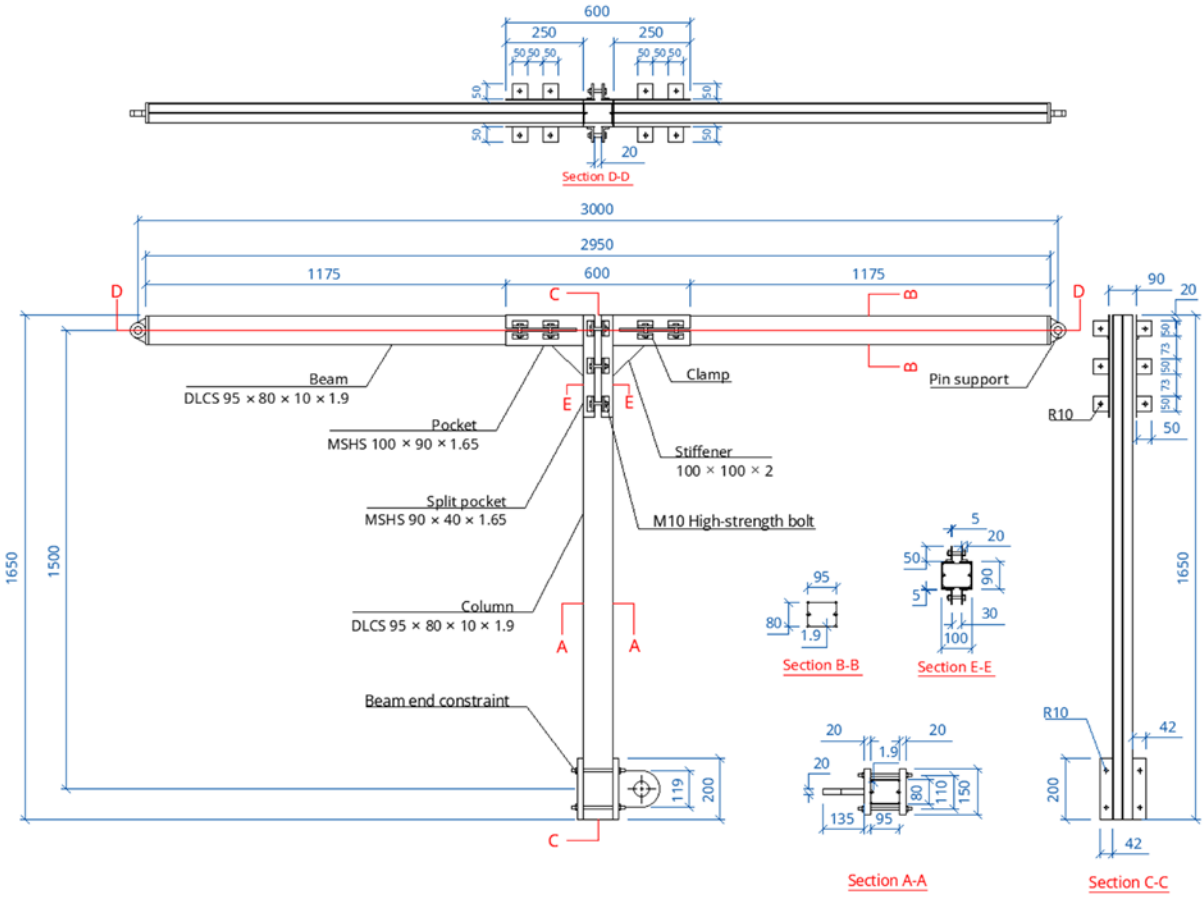

Fig. 3 Typical geometry of the CSPM connection system (unit: mm)

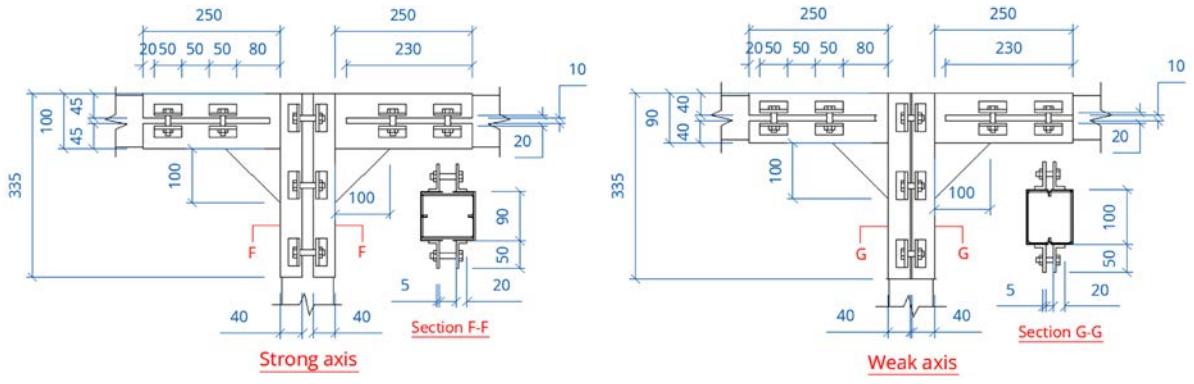

(a) (b)

Fig. 4 Detailed joint dimensions (unit: mm): (a) CSPM-1 and (b) CSPM-2

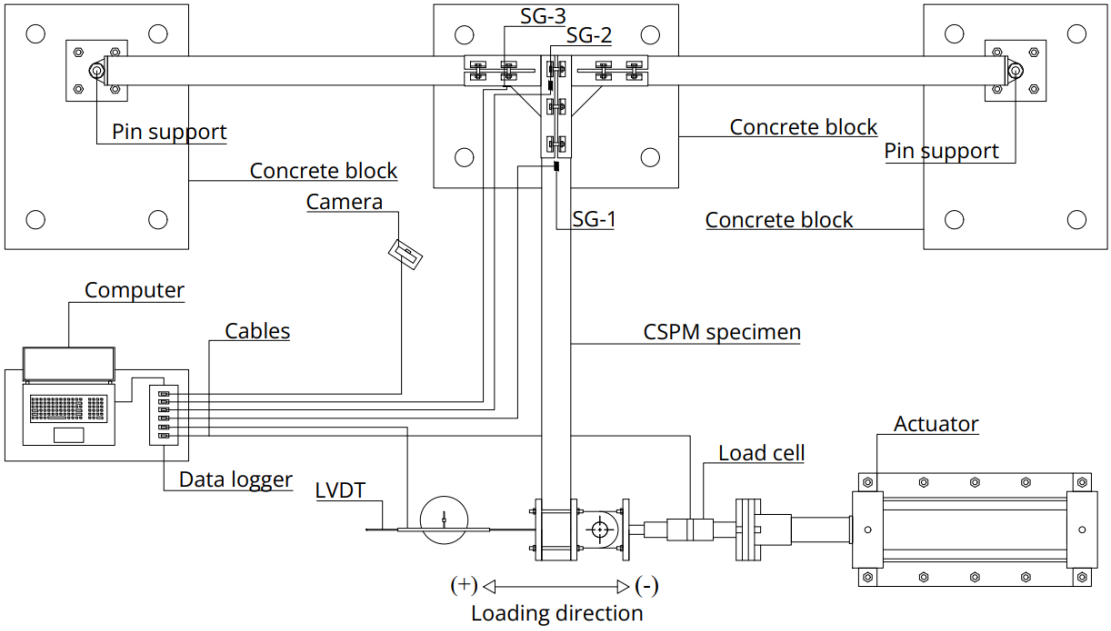

(a) Typical layout of test configuration

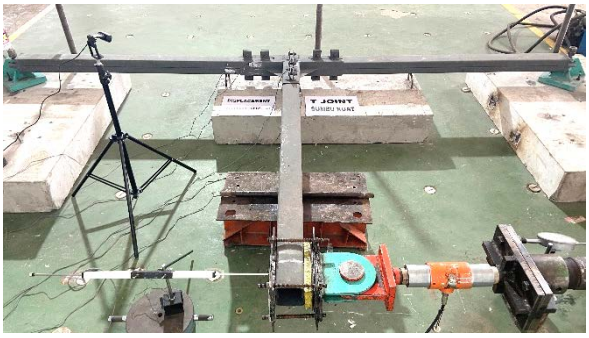

(b) Test configuration of the CSPM-1

(c) Test configuration of the CSPM-2

Fig. 5 Experimental test configuration of the specimens

block. In order to simulate boundary conditions at moment inflection points, the end of both beams was pinned, and one end of the column was clamped to connect with the load cell and actuator. Then, every high-strength bolt was preloaded to 5 kN using a torque wrench with a nut factor of 0.3 [19]. It induced clamping from the pocket to the beams and column. After that, a linear variable differential transformer was placed near the load cell to measure the horizontal displacement of the top-end column. Strain gauges of SG-1 to SG-3 were positioned vertically along the column and beam axes; strain gauge SG-1 was located on the column near the top of the split pocket, and SG-2 to SG-3 were located close to the lower section of the split pocket and stiffener. Fig. 5 also depicts the placement of strain gauges on the specimens. Furthermore, the actuator was loaded horizontally in both the positive and negative directions based on the cyclic loading protocol outlined in AISC 341 [20], as shown in Fig. 6.

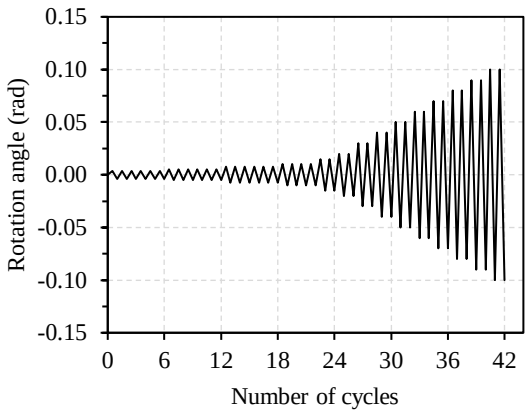

Fig. 6 Cyclic loading protocol for a beam-to-column moment connection [20]

Table 2. Material properties for the specimen's cyclic loading

Component	t (mm)	f_y (MPa)	f_u (MPa)	Elongation (%)
MSHS	1.65	274	355	17.60
DLCS	1.90	280	341	14.98

Primary data such as load, displacement, and strain were collected through a data acquisition tool and monitored on the computer during loading. Finally, the cyclic loading sequence was initially suspended to check the condition of the CSPM specimens upon reaching a drift of 0.04 rad, the lower limit for the seismic force-resisting system as per AISC 314-16. It could then continue beyond this point until the maximum drift of 0.095 rad.

5. RESULT AND DISCUSSION

5.1 Stiffness Evaluation

The stiffness level of the connection was determined using experimental and theoretical results. For the experimental stiffness, the yield criterion for the specimens was utilized, precisely the equal energy method [21], as depicted in Fig. **7**. The experimental stiffness was calculated by dividing the yield load by the yield displacement of the specimen. In contrast, the theoretical stiffness assumed an ideal rigidity for connecting the column and beam components, which was calculated using Eq. (1).

$$\boldsymbol{K_{r,theo} = \frac{2EI}{L^3}} \quad (1)$$

Where E and I represent the elastic modulus and moment of inertia of the beam-column component, respectively; L denotes the distance between the loading point and neutral axis of the beam.

The results obtained from applying different bending axis to the specimens demonstrated that the bending axis had a notable impact on the stiffness of the specimens. Table 3 summarizes the results of the analysis. Comparing the CSPM-1 specimen loaded in the strong axis to the CSPM-2 specimen loaded in the weak axis, the experimental stiffness of the former was found to be higher, with an increase of 19.64% in the positive direction and 13.22% in the negative direction. Moreover, the disparity of both specimens in theoretical stiffness was even more significant, with an increase of 31.38%. In contrast, the stiffness ratio exhibited an opposite trend, with the CSPM-1 specimen having a lower average stiffness ratio than the CSPM-2 specimen, with values of 0.253 and 0.307, respectively. This result is consistent with a previous study on the HSS-to-HSS connection, where the low stiffness ratio was attributed to localized deformation in the connection system due to flexibility [22]. Furthermore, the discrepancies in stiffness can also be attributed to the fact that the higher section capacity of the beam-column component primarily influenced the theoretical stiffness results. In contrast, the experimental stiffness results were affected by the lower section capacity of the split pocket component of the joint.

Another behavior related to the stiffness was the specimens' stiffness degradation during the cyclic loading. The stiffness degradation characteristics can be studied through the secant stiffness parameter (K_s^j), where K_s^j was derived by dividing the maximum lateral load (P_j^i) by the corresponding lateral displacement (Δ_j^i) during the cyclic loading protocol's i^{th} cycle and j^{th} step, as described in Eq. (2).

$$\boldsymbol{K_s^j = \frac{\sum_{i=1}^{n} P_j^i}{\sum_{i=1}^{n} \Delta_j^i}} \quad (2)$$

Fig. 8 depicts that the stiffness degradation of specimens CSPM-1 and CSPM-2 showed the same trend. The stiffness curve took on a curvilinear form, where the stiffness decreased linearly at the beginning, forming a curve at a certain rotation angle. Nonetheless, the stiffness between the positive and negative directions at the beginning of the linear phase had different values in both specimens. Specifically, the stiffness in the positive direction was lower than the negative direction at a rotation angle of 0.004 rad (first step). As the cyclic loading progressed to the rotation angle of 0.005 rad (second step), stiffness in the positive direction spiked. In contrast, the negative direction experienced a drastic decrease in stiffness. This condition is consistent with reported studies in which different values and drastic decreases in stiffness were attributed to the initial slip on the joint components and the asymmetry in the specimen's configuration during cyclic loading [23, 24].

5.2 Hysteretic Behaviors

The hysteretic curve, obtained from the relationship between rotational and moment, provides valuable information about the response of connections. The moment at the joint is calculated by multiplying the applied load by the perpendicular distance to the centroid of the connection. Simultaneously, the rotation angle is determined by dividing the lateral displacement by the moment arm (L_m). Fig. 9 depicts the hysteretic curve of the specimens following cyclic loading.

Both specimens exhibited a similar shape in their hysteretic curves, appearing as a reverse S-shaped curve with pinching in the middle. This result is consistent with the study by Xie et al. [25] and Wu et al. [26], in which the distinctive shape emerged as the

Table 3. Stiffness of the specimens

Specimen	Loading direction	P_y (kN)	P_u (kN)	D_y (mm)	D_u (mm)	$K_{e,exp}$ (kN/m)	$K_{r,theo}$ (kN/m)	$K_{e,exp}/K_{r,theo}$
CSPM-1	Positive	2.65	3.15	82.62	135.32	32.08	113.23	0.283
	Negative	2.52	2.92	100.26	142.64	25.11	113.23	0.222
CSPM-2	Positive	2.10	2.49	81.57	135.13	25.78	77.56	0.332
	Negative	2.00	2.38	91.97	142.63	21.79	77.56	0.281

Note: P_y represents yield load, P_u represents ultimate load, D_y represents yield displacement, D_u represents ultimate displacement, $K_{e,exp}$ represents experimental effective stiffness, and $K_{r,theo}$ represents theoretical stiffness.

specimens experienced a simultaneous increase in lateral force and a decrease in stiffness during cyclic loading. The decrease in stiffness in both specimens began at a rotation angle of 0.007 rad (third step), with no evidence of plastic deformation observed at this rotation angle. Subsequently, the decreased stiffness persisted until the completion of cyclic loading at a rotation angle of 0.095 rad. Consequently, the contrasting relationship between lateral force and rigidity is likely attributable to the joint system becoming more flexible with the increase in applied rotation angle.

The pinching effect observed in the hysteretic curves involved the narrowing of the transition region between the positive and negative directions of the curve. Kordzangeneh et al. [27] showed that narrowing in the hysteretic curve results from stiffness reduction and subsequent stiffness recovery during cyclic loading. This condition is caused by the buckling phenomenon in the specimen [27, 28]. Accordingly, CSPM-1 and CSPM-2 also exhibited a similar condition where the local buckling occurred in the flange of the split pocket near the face of the beam. This area acted as a support region, making it susceptible to stress or strain concentration. Therefore, the flanges of the split pocket experienced inelastic deformation in their outer fibers, leading to local buckling in both specimens.

In addition, the primary difference between both specimens lay in their patterns of strength degradation. Based on the hysteretic curve presented in Fig. 9, it was observed that CSPM-1 began experiencing strength degradation at a rotation angle of 0.095 rad, whereas the strength degradation pattern for CSPM-2 remained imperceptible. Accordingly, the CSPM-2 specimen retained the potential to achieve a higher deformation capacity compared to CSPM-1.

5.3 Skeleton Curves

Fig. 10 compares the skeleton curves of the two specimens. Initially, the moment-rotation curves for CSPM-1 and CSPM-2 exhibited similar patterns. When both specimens attained a rotation angle of 0.02 rad, the difference in their bending axis began to influence their moment capacity. Compared with CSPM-2, the yield moment capacity of CSPM-1 increased by 20.85% in the positive direction and 20.37% in the negative direction. CSPM-1 showed an increase of 21.14% in the positive direction and an increase of 18.49% in the negative direction at the ultimate moment capacity. Therefore, CSPM-1 exhibited a higher yield and ultimate moment capacity than CSPM-2. Conversely, the disparity of the yield rotation angle between CSPM-1 and CSPM-2 showed a similar trend with the moment capacity but with a low percentage. Compared to the CSPM-2, the CSPM-1 demonstrated a yield rotation angle that increased by 1.81% and 8.95% in the positive and negative directions, respectively. Furthermore, the ultimate rotation angle remained relatively unaffected between the two configurations. These results indicate that the loading applied to the specimens impacts the moment capacity more than the rotation angle.

The level of restraint in the connection could influence the disparity response of specimens in moment capacity and rotation angle. According to AISC 341 [20], the classification of a connection as fully restrained (FR) or partially restrained (PR) depends on the comparison between the connection's maximum moment capacity ($\boldsymbol{M_{max} = P_u L_m}$), determined through testing, and the theoretical plastic moment capacity of the connected column ($\boldsymbol{M_{p,col} = f_y Z}$). The maximum moment capacity of the CSPM (specific term for CSPM) connection was obtained at the ultimate load, multiplied by the moment arm of the connection system. Table 4 summarizes the detailed results of the classification. The CSPM-1 and CSPM-2 joints were categorized as Partially Restrained (PR) because the maximum moment (M_{max}) of each joint was lower than the column's theoretical plastic moment ($M_{p,col}$), but not less than half. Furthermore, the CSPM-1 and CSPM-2 joints were categorized as ordinary moment frames (OMF) because their moment capacity at rotation angles of 0.02 rad and 0.04 rad did not surpass 80% of their maximum moment capacity [20]. This condition was due to the plastic deformation caused by inelastic local buckling in their split pockets, which resulted in faster degradation of the connection's moment capacity before reaching the lower limit of the column's plastic moment. Nevertheless, the prefabricated instant steel house

Table 4. The result of restraint category and moment frame system

Specimen	Loading direction	M_{max} (kN.m)	$M_{p,col}$ (kN.m)	Restraint category	$M_{0.02rad}$ (kN.m)	$M_{0.04rad}$ (kN.m)	$0.8M_{max}$ (kN.m)	Moment frame system
CSPM-1	Positive	4.73	6.89	PR	2.25	3.44	3.78	OMF
	Negative	4.38	6.89	PR	1.78	2.69	3.50	OMF
CSPM-2	Positive	3.73	5.50	PR	1.79	2.72	2.98	OMF
	Negative	3.57	5.50	PR	1.59	2.34	2.85	OMF

Note: M_{max} represents maximum moment capacity, and $M_{p,col}$ represents the column's theoretical plastic moment, $M_{0.02rad}$ represents the moment at 0.02 rad, and $M_{0.04rad}$ represents the moment at 0.04 rad

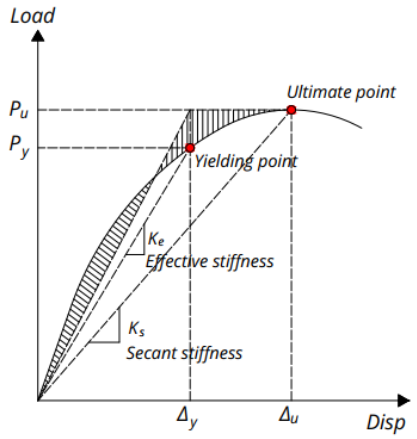

Fig. 7 Definition of yielding point and stiffness

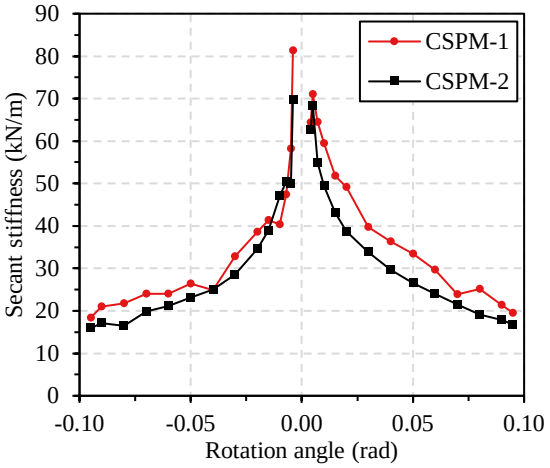

Fig. 8 Stiffness degradation of the specimens

with the OMF steel connection system could still be used in earthquake-prone areas with seismic design categories D, E, and F as long as the structural height remained under 20 m [29]. This was demonstrated by the ability of the connection specimens to rotate beyond 0.04 rad in both directions while maintaining sufficient and stable lateral resistance up to 0.095 rad.

5.4 Energy Dissipation

Ductility is the ability of a material to deform and absorb energy without losing its integrity. In the case of steel joints, the ductility was quantified through a rotational ductility coefficient until the maximum drift of 0.095 rad, as described in Eq. (3).

$$\mu = \frac{\theta_{max}}{\theta_{yield}} \tag{3}$$

where θ_{max} denotes the maximum rotation angle, and θ_{yield} represents the yield rotation angle.

The rotational ductility coefficients of CSPM-1 and CSPM-2 ranged from 1.42 to 1.75. According to Table 5, CSPM-2 demonstrated a slightly higher ductility coefficient than CSPM-1, with a disparity of 1.16% in the positive direction and 9.15% in the negative direction. This difference could be attributed to the fact that CSPM-2 undergoes plastic deformation earlier than CSPM-1, thereby enhancing its ability to generate plastic deformation in the connection system. Plastic deformation occurred in the same area in both specimens, specifically on the flange of the split pocket near the beam's face. The local buckling effect amplified the presence of plastic deformation in this location. The formation of plastic deformation has a positive impact on the absorption of seismic energy, as demonstrated by Zhang, Xu and Li [11]. Therefore, plastic deformation helps to prevent brittle failure and mitigate severe damage to the CSPM connection system.

5.5 Energy Dissipation

Jacobsen's approach [30] demonstrates the crucial capability to dissipate energy in characterizing seismic performance through hysteretic energy dissipation (E_d) and the equivalent viscous damping coefficient (h_e). Hysteretic energy dissipation and equivalent viscous damping coefficient represent the amount of damping in the joint because of various mechanisms, such as material inelasticity and connection configuration. The two parameters can be assessed using Eqs. (4) and (5).

$$E_d = \sum_{i=0}^{n} \frac{(F_{(i+1)} + F_i)}{2} (\Delta_{(i+1)} + \Delta_i) \tag{4}$$

$$h_e = \frac{1}{2\pi} \cdot \frac{E}{A_{(OAE)} + A_{(ODF)}} \tag{5}$$

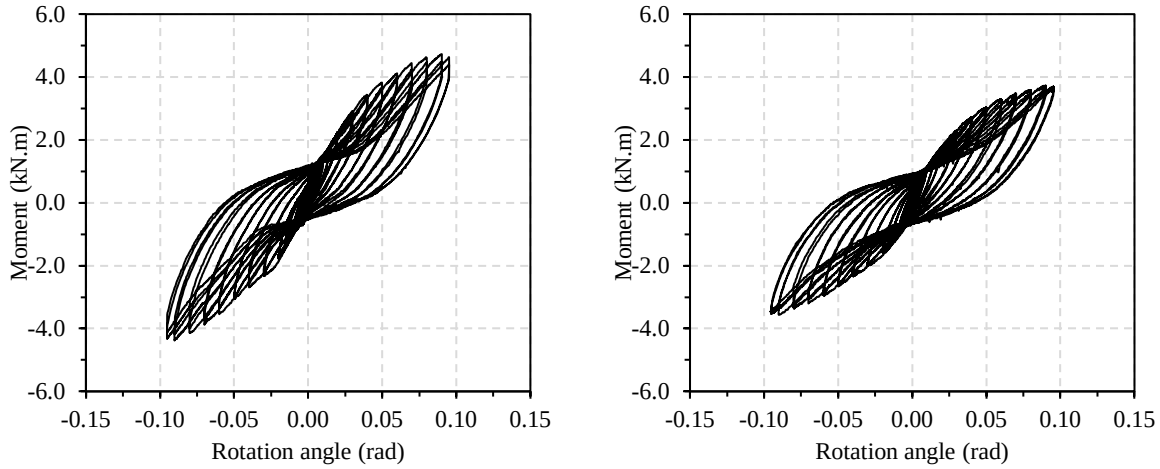

Fig. 9 The hysteretic curve of the specimens: (a) CSPM-1, (b) CSPM-2

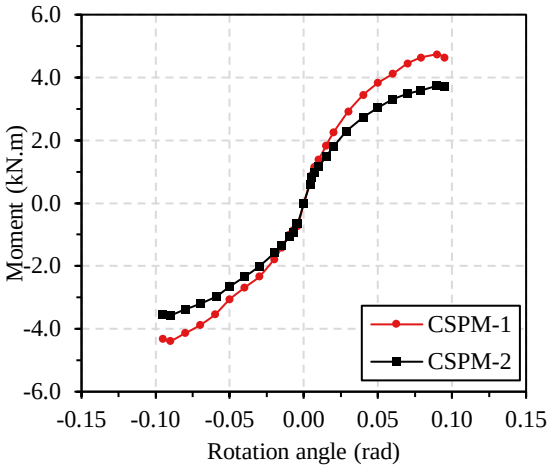

Fig. 10 Skeleton curve of the specimens

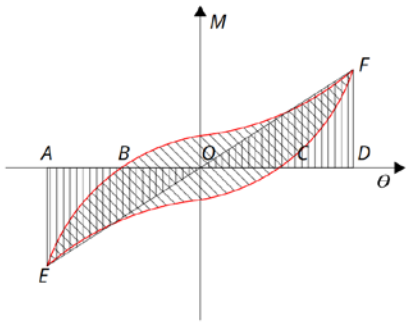

Fig. 11 Definition of a hysteretic loop

Where F represents the force; Δ represents the displacement at a specific point; $A_{(BECFB)}$ refers to the hysteretic loop at the loading step, as shown in the shaded region of Fig. 11; $A_{(OAE)}$ represents the area of triangle OAE, and $A_{(ODF)}$ refers to the area of triangle ODF.

Fig. 12 shows that the ability to dissipate earthquake energy in the CSPM-1 specimen was higher than in the CSPM-2. This difference appeared higher than in the CSPM-2. This difference appeared

Table 5. Ductility coefficient

Specimen	Loading direction	θ_y (rad)	θ_{max} (rad)	μ
CSPM-1	Positive	0.055	0.095	1.73
	Negative	0.067	0.095	1.42
CSPM-2	Positive	0.054	0.095	1.75
	Negative	0.061	0.095	1.55

when the two joint specimens reached a rotation angle of 0.02 rad. Then, the energy dissipation capacity increased gradually as the rotation angle increased. The CSPM-1 could also generate more stiffness and strength than the CSPM-2 because it was loaded in the strong axis, thereby resulting in a higher energy dissipation capacity. The energy dissipation capacity decreased when the rotation angle reached 0.090 rad owing to the limited length of the actuator's piston rod.

Following the above conditions, the CSPM-1 had a relatively higher and fluctuating equivalent viscous damping coefficient than the CSPM-2. However, both specimens had a similar trend of increasing the equivalent viscous damping coefficient at the beginning until the rotation angle reached 0.025 rad. When the rotation angle reached 0.035 rad, the equivalent viscous damping coefficient values of the CSPM-1 specimen began to decrease until the end of the loading process. By contrast, the CSPM-2 specimens tended to produce the equivalent viscous damping coefficient as the rotation angle increased. This condition indicated that the connection system did not undergo additional plastic deformation during only occurred in the flange part of the split pocket.

5.6 Strain Analysis

The installation locations of the strain gauges in the test specimen are depicted in Fig. 5. Strain gauge

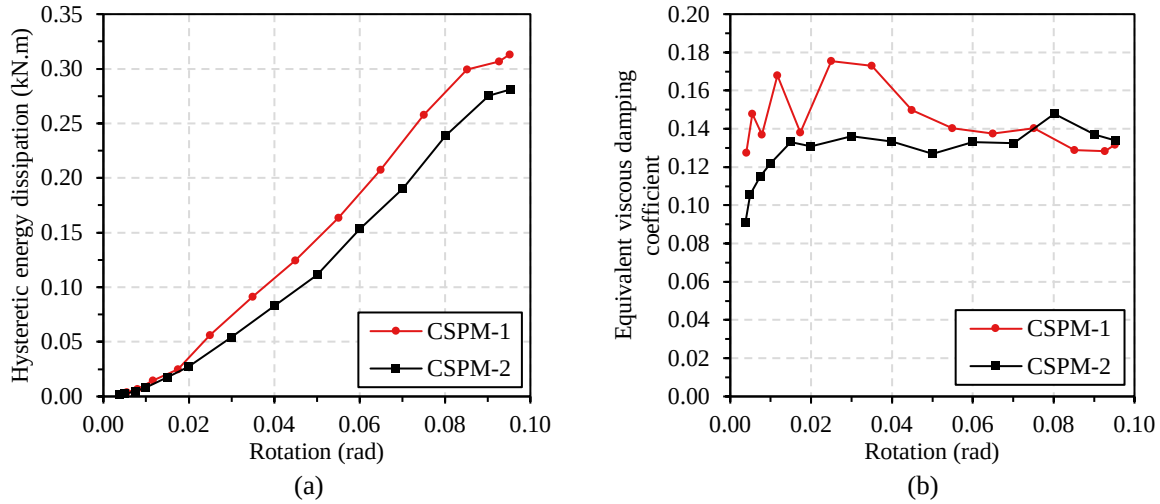

Fig. 12 Energy dissipation capacity for each rotation angle: (a) Energy dissipation capacity of the specimens and (b) Equivalent viscous damping coefficient of the specimens

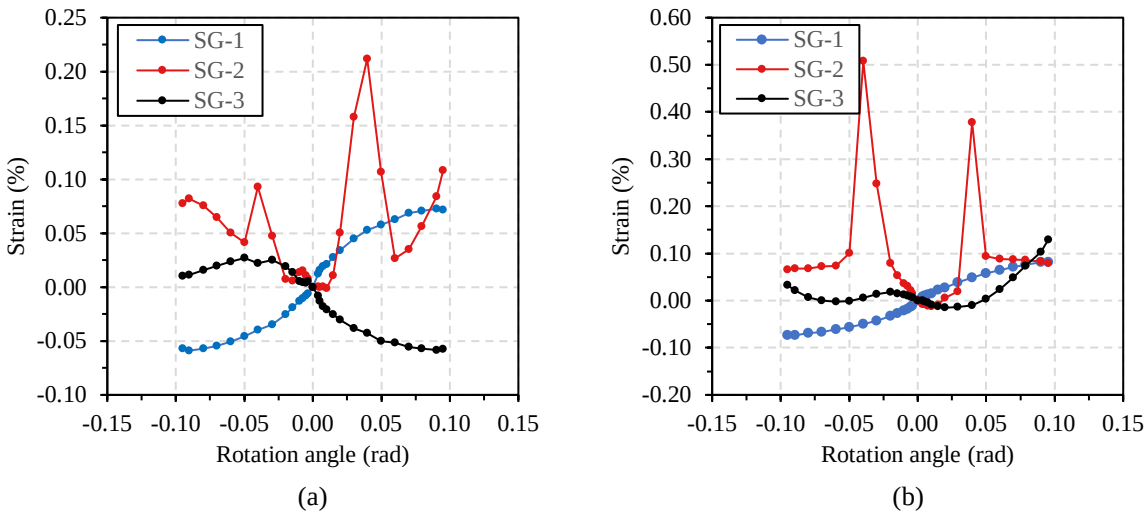

Fig. 13 Strain under cyclic loading: (a) CSPM-1 and (b) CSPM-2

SG-1 was positioned on the column, while strain gauges SG-2 and SG-3 were placed in the split pocket and pocket, respectively. The strain values depicted in Fig. 13 represent the strain values attained when the hysteretic curve reached the maximum rotation angle during each step of the cyclic loading protocol. According to the coupon test results, the yield strain values for the joint and beam-column components were 0.14% and 0.15%, respectively. Fig. 13 depicts the strain curves of strain gauges SG-1, SG-2, and SG-3 on specimens CSPM-1 and CSPM-2 under cyclic loading. SG-2 reached the yield strain, while SG-1 and SG-3 remained within the elastic range concerning the yield strain. This occurred because SG-2 was positioned directly above the flange of the split pocket, which experienced inelastic local buckling. When inelastic local buckling occurred at a specific location, it induced a shift in stress concentration, thereby propagating inelastic local buckling to adjacent locations. This condition caused a spike to a certain value in the strain curve of strain gauge SG-2. In CSPM-1, SG-2 reached the yield strain at a rotation angle of 0.040 rad, with a corresponding strain value of 0.21%. In CSPM-2, SG-2 reached the yield strain at a rotation angle of −0.030 rad, with a strain value of 0.25%. These observations were consistent with the observation during the experiment, where both CSPM-1 and CSPM-2 exhibited inelastic local buckling at the flange of the split pocket, as shown in
Fig. 14. At the same time, the column and beam remained undamaged.

5.7 Failure Modes

The failure modes observed in the specimens provided a detailed understanding of the behavior of

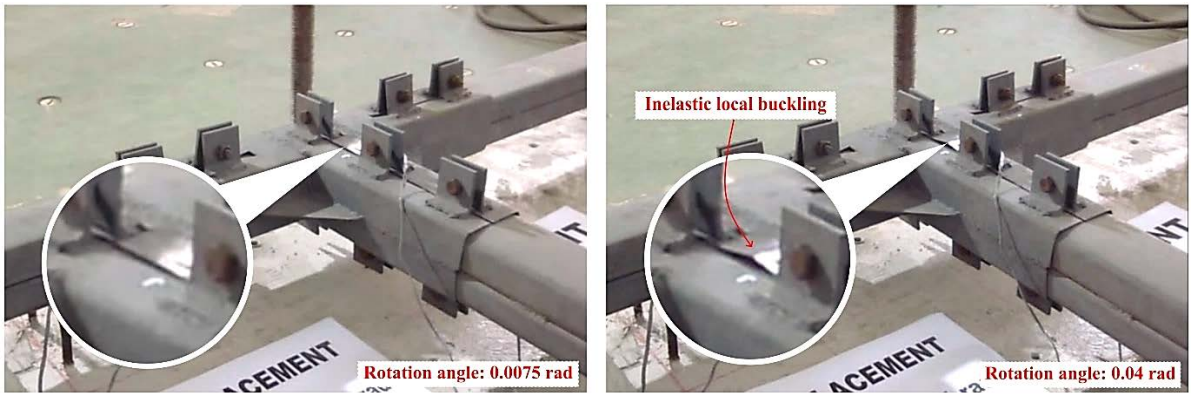

(a)

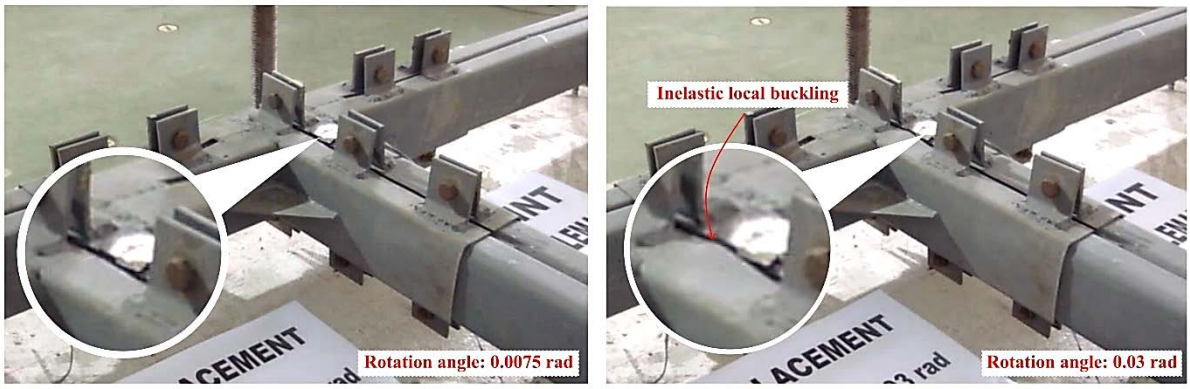

(b)

Fig. 14 Flange form of the split pocket before and after inelastic local buckling: (a) CSPM-1 and (b) CSPM-2

the CSPM connection system. Fig. 15 illustrates the failure modes of CSPM-1 and CSPM-2 after they had reached full cyclic loading. In the case of CSPM-1, when a loading rotation angle of 0.040 rad was obtained in both loading directions, inelastic local buckling developed on the flanges of the split pocket near the face of the beam. Conversely, CSPM-2 also experienced inelastic local buckling at the same area as CSPM-1 but at a smaller rotational angle of 0.030 rad and −0.030 rad, occurring at the exact location as CSPM-1. One of the stiffeners welded to the pocket experienced weld fracture while the CSPM-1 specimen rotated at an angle of −0.06 rad. Beyond this rotation angle, no further signs of failure were detected in the specimens till the completion of cyclic loading. Upon completion of the cyclic loading protocol, examination revealed the formation of inelastic local buckling in the out-of-plane direction, with an approximate magnitude of 11 mm. This buckling occurred symmetrically on the flange of the split pocket, as depicted in Fig. 15.

These failures were primarily caused due to the concentration of stress at the location of their occurrences. Stress concentration developed due to the redistribution of stress in the joint system of the CSPM when the joint underwent cyclic loading. When the specimen was loaded in the positive direction, both the positive and negative sides of the flanges of the split pocket simultaneously experienced tensile and compressive stresses. If the compressive stress surpassed the yield strength of the outer fiber and the compressive strength of the split pocket's cross-section, local buckling happened on the flange of the negative side. Furthermore, the slenderness of the split pocket flange played a role in triggering local buckling failure.

Moreover, the end of the stiffener on the negative side encountered an intensified concentration of tensile stress as the applied lateral load increased. When the tensile stress surpassed the tensile strength of the weld, the weld fractured. However, this weld failure only occurred on the positive side of the CSPM-1 specimen. This situation appeared to result from the asymmetrical configuration of the CSPM joint, which affected the moment distribution on both positive and negative sides shown in Fig. 9, consistent with the asymmetrical behavior of interlocking inter-module connection studied by Lacey et al. [31]. Although the CSPM-1 and CSPM-2 specimens had similar configurations, the CSPM-1 specimen exhibited more substantial localized damage, while the column and beam remained relatively undamaged.

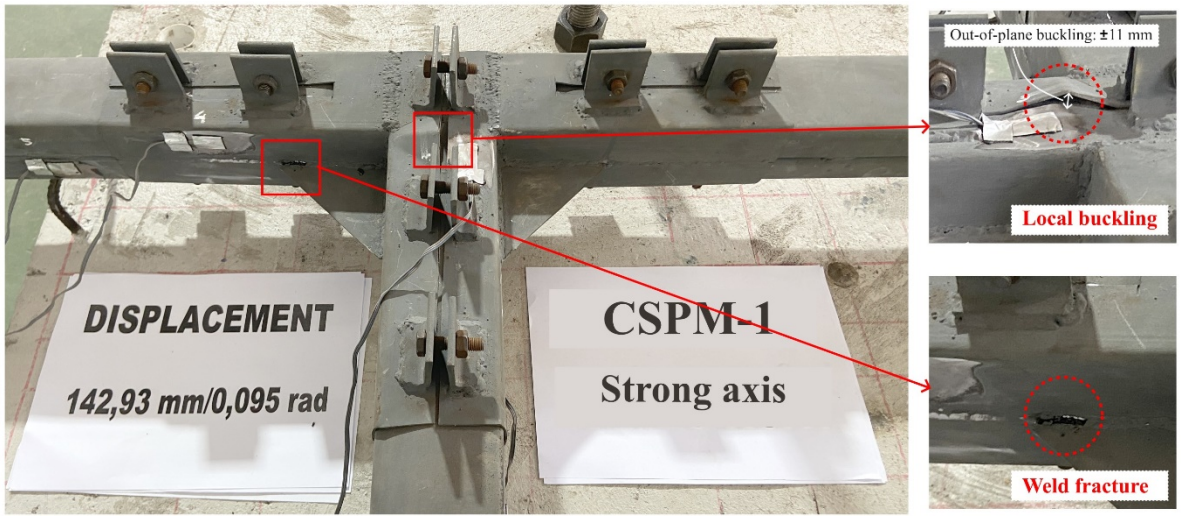

(a)

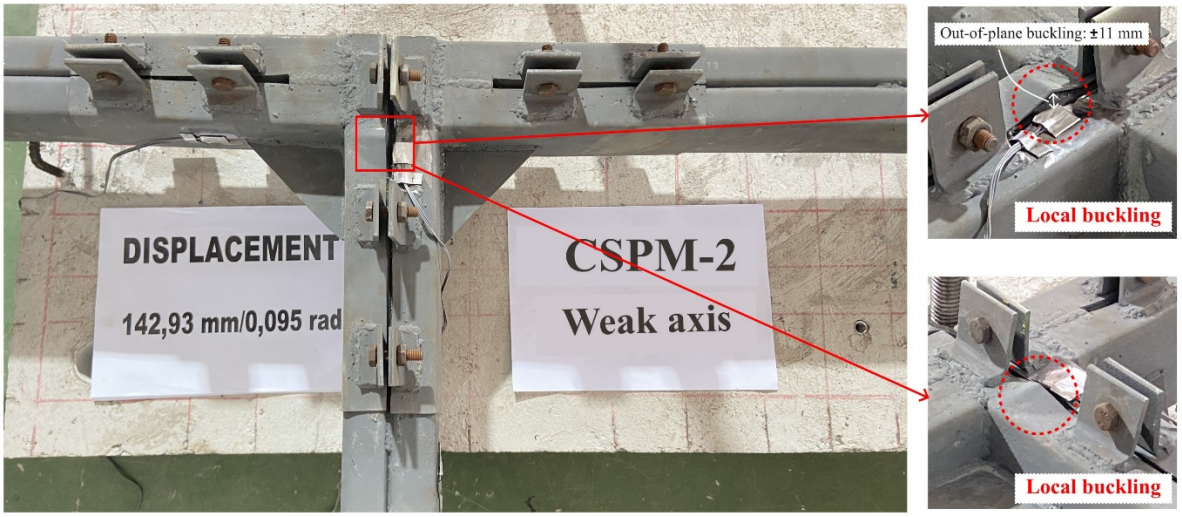

(b)

Fig. 15 Failure modes of the specimens: (a) CSPM-1 and (b) CSPM-2

6. CONCLUSION

This study proposed CSPM as a beam-column joint system. The CSPM eliminates the need for on-site welding by utilizing a plug-and-play connection system between the beam-column and pockets, followed by a clamping mechanism induced by preloaded fasteners. The key findings from this study can be summarized as follows:

1. The CSPM exhibited a hysteretic response with a reversed S-shaped curve and a pinching in the middle. Inelastic local buckling within the split pocket was crucial in generating plastic deformation. This deformation was essential in absorbing seismic energy, effectively preventing brittle failure and remarkably reducing damage to the joint system. The observed failure modes in the connection system were primarily caused by inelastic local buckling on the flanges of the split pocket and weld fracture on one of the stiffeners. Finally, the CSPM proved its dependability as a prefabricated beam-column joint system for a one-story instant steel house.
2. The bending axis and splitting considerably affect the CSPM connection system. The bending axis, specifically the strong axis, possesses greater stiffness, a higher moment capacity, and effective energy dissipation capabilities. Conversely, splitting causes local buckling on the flange of the divided pocket, which can have various effects. It can mitigate damage to the joint system but at the expense of its lateral capacity.
3. All CSPM specimens demonstrated adequate and stable lateral resistance up to 0.04 rad in both positive and negative loading directions without brittle failure indications. The ductility

coefficients of the CSPM specimens ranged from 1.42 to 1.75 owing to their rotational ability.

4. Compared to the theoretical plastic moments of the column, the maximum moment capacity of the CSPM specimens was lower but still greater than half. When the rotation angle reached 0.02 radians, none of the specimens achieved a moment capacity exceeding 80% of the maximum moment capacity of the column. Consequently, the CSPM specimens were classified as PR and OMF.
5. The CSPM connection system generally meets the standards for use in a one-story building because it can achieve sufficient lateral resistance in large deformation. However, further study of pocket length and thickness variables is still necessary to obtain practical equations for designing the CSPM connection system more easily. This can be achieved by comparing the experimental results with numerical modeling using finite element analysis. Using database results of the numerical modeling could be used to develop the equation for the CPSM design.

7. ACKNOWLEDGEMENTS

The authors would like to thank the Research Directorate of Universitas Gadjah Mada for their support (Grant Number 5075/UN1.P.II/Dit-Lit/PT.01.01/2023) and the Structural and Building Material Laboratory, Department of Civil and Environmental Engineering, Faculty of Engineering, Universitas Gadjah Mada for facilitating the experimental testing process. We are also grateful to the Badan Penerbit dan Publikasi Universitas Gadjah Mada for their invaluable assistance in editing this manuscript. The CSPM connection system was also registered under a patent with registration number P00202200431.

8. REFERENCES

[1] Fajar, A. S., Saputra, A., Satyarno, I., Himawan, L., Investigation of fast connection (clamped pocket mechanics) for modular instant steel house with finite element analysis: back to build post-disaster, in Proc. 5th Int. Conf. on Sustainable Civil Engineering Structures and Construction Materials, Vol. 215, 2022, pp. 767–785.

[2] Sutrisno, W., Satyarno, I., Awaludin, A., Saputra, A., Setiawan, A. F., Seismic performance of instant steel frame house for post earthquake reconstruction, in Proc. 5th Int. Conf. on Sustainable Civil Engineering Structures and Construction Materials, Vol. 215, 2022, pp. 81-97.

[3] Bazarchi, E., Davaran, A., Lamarche, C. P., Roy, N., Parent, S., Experimental and numerical investigation of a novel vertically unconstrained steel inter-modular connection, Thin-Walled Struct., Vol. 183, 2023, 110364.

[4] Qin, J., Tan, P., Design method of innovative box connections for modular steel constructions, J. Build. Eng., Vol. 57, 2022, 104820.

[5] Zhang, G., Xu, L. H., Xie, X. S., Haunch connecting techniques in a self-centering modular steel structure connection system, J. Build. Eng., Vol. 62, 2022, 105389.

[6] Rajanayagam, H., Gunawardena, T., Mendis, P., Pologanathan, K., Gatheeshgar, P., Dissanayake, M., et al., Evaluation of inter-modular connection behaviour under lateral loads: An experimental and numerical study, J. Constr. Steel Res., Vol. 194, 2022, 107335.

[7] Srisangeerthanan, S., Hashemi, M. R., Hashemi, M. J., Rajeev, P., Gad, E., Fernando, S., Review of performance requirements for inter-module connections in multi-story modular buildings, J. Build. Eng., Vol. 28, 2020, 101087.

[8] Deng, E.-F., Zong, L., Ding, Y., Zhe, Z., Zhang, J.-F., Fengwei, S., et al., Seismic performance of mid-to-high rise modular steel construction - A critical review, Thin-Walled Struct., Vol. 155, 106924.

[9] Nadeem, G., Safiee, N. A., Bakar, N. A., Karim, I. A., Nasir, N. A. M., Connection design in modular steel construction: A review, Structures, Vol. 33, 2021, pp. 3239-3256.

[10] Thai, H.-T., Ngo, T., Uy, B., A review on modular construction for high-rise buildings, Structures, Vol. 28, 2020, pp. 1265-1290.

[11] Zhang, G., Xu, L.-H., Li, Z.-X., Experimental evaluation on seismic performance of a novel plug-in modular steel structure connection system, Eng. Struct., Vol. 273, 2022, 115099.

[12] Cabaleiro, M., Conde, B., Riveiro, B., Caamaño, J. C., Analysis of steel connections with girder clamps according to the bolts preload, J. Constr. Steel Res., Vol.168, 2020, 105866.

[13] Luo, F. J., Fu Jia Luo, Fu Jia Luo, Chenting Ding, Chenting Ding, Ding, C., et al., End plate–stiffener connection for SHS column and RHS beam in steel-framed building modules, Int. J. Steel Struct., Vol. 19, Issue 4, 2019, pp. 1353-1365.

[14] Chen, Z., Liu, J., Yu, Y., Zhou, C., Yan, R., Experimental study of an innovative modular steel building connection, J. Constr. Steel Res., Vol. 139, 2017, pp. 69-82.

[15] Ma, R., Xia, J., Chang, H., Xu, B., Zhang, L., Experimental and numerical investigation of mechanical properties on novel modular connections with superimposed beams, Eng. Struct., Vol. 232, 2021, 111858.

[16] Nadeem, G., Safiee, N. A., Abu Bakar, N., Abd Karim, I., Mohd Nasir, N., A. Finite Element Analysis of Proposed Self-Locking Joint for Modular Steel Structures, Appl. Sci., Vol. 11. Issue 19, 2021, 9277.

[17] Khan, K., Yan, J.-B., Finite Element Analysis on Seismic Behaviour of Novel Joint in Prefabricated Modular Steel Building, Int. J. Steel Struct., Vol. 20, Issue 3, 2020, pp. 752-765.

[18] JIS Z 2241, Metallic Materials – Tensile Testing – Method of Test at Room Temperature, Japanese Standards Association, 2011.

[19] Budynas, R. G., Nisbett, J. K., Shigley's Mechanical Engineering Design, 10th ed., McGraw-Hill Education, New York, 2015, pp. 429-431.

[20] AISC 341, Seismic Provisions for Structural Steel Buildings, American Institute of Steel Construction, 2016.

[21] Lu, S., Wang, Z., Pan, J., Wang, P., The Seismic Performance Analysis of Semi-rigid Spatial Steel Frames Based on Moment-Rotation Curves of End-plate Connection, Structures, Vol. 36, 2022, pp. 1032–1049.

[22] Fadden, M., Wei, D., McCormick, J., Cyclic Testing of Welded HSS-to-HSS Moment Connections for Seismic Applications, J. Struct. Eng.-Asce, Vol. 141, Issue 2, 2015, 04014109.

[23] Lacey, A. W., Chen, W., Hao, H., Bi, K., New interlocking inter-module connection for modular steel buildings: Experimental and numerical studies, Eng. Struct., Vol. 198, 2019, 109465.

[24] Yu, Y., Zhang, A., Pan, W., Mou, B., Liu, X., Seismic performance of beam-column connections with welded upper flange and bolted lower flange, J. Constr. Steel Res., Vol. 182, 2021, 106697.

[25] Xie, Q., Wang, L., Zhang, L., Xiang, W., Hu, W., Rotational Behaviors of Fork-Column Dou-Gong: Experimental Tests and Hysteresis Model. J. Perform. Constr. Facil., Vol. 34, Issue 3, 2020, 04020032.

[26] Wu, Z., Tao, Z., Liu, B., Zuo, H., Experimental study on all-bolted joint in modularized prefabricated steel structure, Struct. Eng. Mech., Vol. 73, Issue 6, 2020, pp. 613-620.

[27] Kordzangeneh, G., Showkati, H., Rezaeian, A., Yekrangnia, M., Experimental cyclic performance of steel shear walls with single rectangular opening, Struct. Des. Tall Spec. Build., Vol. 30, Issue 2, 2021, 1821.

[28] Sabouri-Ghomi, S., Gholhaki, M., Tests of two three-story ductile steel plate shear walls, 2012, pp. 1-12.

[29] FEMA P-1050-1, NEHRP Recommended Seismic Provisions for New Buildings and Other Structures, FEMA, 2015.

[30] Heitz, T., Giry, C., Richard, B., Ragueneau, F., Identification of an equivalent viscous damping function depending on engineering demand parameters, Eng. Struct., Vol. 188, 2019, pp. 637–649.

[31] Lacey, A. W., Chen, W., Hao, H., Bi, K., New interlocking inter-module connection for modular steel buildings: Simplified structural behaviours, Eng. Struct., Vol. 227, 2021, 111409.